metals

MDPI

Article

Microstructural Evolution and Work-Hardening Behaviour in a High-Nitrogen Nickel-Free Stainless Steel

Marine Barrabé [1,2], Frédéric Prima [1] and Stéphanie Delannoy [1,2,*]

[1] Chimie ParisTech, CNRS, Institut de Recherche de Chimie Paris, PSL Research University, 75005 Paris, France
[2] Biotech Dental SAS, 305 Allées de Craponne, 13300 Salon-de-Provence, France
* Correspondence: stephanie.delannoy@chimieparistech.psl.eu

Abstract

Nickel-free high-nitrogen austenitic stainless steels (HNSS) are increasingly considered for biomedical applications owing to their excellent biocompatibility, corrosion resistance, and favourable mechanical properties. Their mechanical behaviour is strongly influenced by interstitial alloying, which can enhance both strength and work-hardening capability. However, the deformation mechanisms governing work hardening in HNSS, particularly at high nitrogen contents, remain insufficiently understood. Here, we investigate the effect of nitrogen on the mechanical response and associated deformation mechanisms of a nickel-free austenitic stainless steel containing 1 wt.% nitrogen. Tensile tests revealed a combination of high strength, sustained work hardening, and good ductility, with further strengthening achievable through cold rolling. The annealed material exhibited a distinct constant strain-hardening regime during the early stages of deformation. Using electron backscatter diffraction and in situ tensile testing, planar dislocation slip, evidenced by slip traces, was identified as the predominant deformation mechanism, with no detectable strain-induced martensitic transformation or mechanical twinning in this regime. Mechanical twinning was observed only at higher strains (>15%) and appears to make a secondary, limited contribution to the overall deformation. Despite the relatively high calculated stacking-fault energy, the mechanical and microstructural observations are consistent with strongly restricted cross-slip and localized dislocation glide. These findings suggest that chemical short-range order may play an important role in governing the distinctive plasticity and sustained work-hardening behaviour of Ni-free HNSS.

Keywords: high-nitrogen stainless steel; in-situ tensile testing; electron backscatter diffraction (EBSD); work hardening; planar slip

Academic Editors: Nuria Pulido González and Victoria Bonache Bezares

Received: 2 October 2026
Revised: 3 November 2026
Accepted: 10 November 2026
Published: 12 November 2026

Copyright: © 2026 by the author. Licensee MDPI, Basel, Switzerland. This article is an open access article distributed under the terms and conditions of the Creative Commons Attribution (CC BY) license.

1. Introduction

In the past few years, high-nitrogen stainless steels (HNSS)—alloys in which nitrogen acts as a key interstitial element—have attracted increasing attention across a wide range of sectors, including the chemical, energy, aerospace, and, more recently, biomedical industries [1–4]. This growing interest arises from their distinctive combination of properties. Owing to its strong austenite-stabilizing effect, nitrogen significantly extends the γ-phase stability domain while providing pronounced solid-solution strengthening. As a result, HNSS exhibit superior mechanical performance compared to conventional

austenitic stainless steels, such as 316L, including higher yield strength and enhanced fatigue resistance [5–7].

Nitrogen-stabilized austenite ensures non-magnetic behaviour, which is required for compatibility with magnetic resonance imaging (MRI), and enables the reduction or elimination of nickel, which otherwise serves as a γ-stabilizer in conventional steel compositions. This aspect is of increasing importance in light of concerns related to nickel-induced hypersensitivity [8–10]. Due to the beneficial effect of nitrogen, HNSS have also been reported to exhibit corrosion resistance that significantly surpasses that of standard 316L stainless steel [4,11–13]. This contributes to limiting metal ion release in physiological environments, thereby improving biocompatibility and long-term biological safety [14,15].

In addition, their relatively high elastic modulus and good wear resistance make HNSS promising candidates for applications requiring high stiffness, which are currently fulfilled by cobalt–chromium alloys. This is particularly relevant in the context of already started regulatory restrictions on cobalt-containing materials [16]. Overall, due to their unique combination of properties, HNSS—and especially austenitic nickel-free grades—appear as promising alternatives to conventional reference alloys for medical applications.

Despite the growing body of literature devoted to HNSS, the role of nitrogen in governing deformation mechanisms and mechanical properties remains insufficiently clarified. While its solid-solution strengthening effect is well established, its influence on fundamental plasticity mechanisms—such as dislocation glide, planar slip, and deformation twinning—remains a matter of ongoing debate [17–21]. In particular, the effect of nitrogen on stacking fault energy (SFE), a key parameter controlling the transition between slip-dominated and twinning-assisted plasticity, is still inconsistently reported [22,23]. Contradictory trends are frequently observed across studies, both in terms of the magnitude and the direction of the reported SFE variations [24–27].

These discrepancies are commonly attributed to differences in alloy chemistry, notably the interactions between nitrogen and substitutional elements such as Cr, Mn, and Mo [28–30]. This arises partly from the strong affinity between N and Cr, which promotes short-range ordering (SRO) and favours certain deformation mechanisms over others [31–34]. In addition, the wide range of nitrogen contents investigated—from low interstitial levels to highly supersaturated solid solutions—likely leads to distinct deformation responses [7,35,36]. Further complexity comes from variations in processing routes, grain size, and testing conditions (strain rate, temperature…), all of which strongly influence the active deformation mechanisms [37–39]. Consequently, a unified understanding of the structure–property relationships in nitrogen-alloyed stainless steels is still lacking.

The present study focuses on BioDur® 108 alloy, a nickel-free austenitic HNSS developed by Carpenter Technology Corporation, characterized by a particularly high nitrogen content (up to 1.1 wt.%) [40] and exhibiting attractive mechanical properties. Despite its potential for demanding biomedical applications, the relationships between its microstructure and mechanical behaviour remain only partially understood [41,42]. The objective of this work is to provide a deeper understanding of the role of nitrogen in governing the mechanical behaviour and underlying deformation mechanisms in this specific system. To this end, particular attention is devoted to the characterization of deformation-induced microstructural evolution, notably through in-situ electron backscatter diffraction (EBSD) analysis during tensile loading. This approach is complemented by a detailed investigation of the mechanical response, with specific emphasis on strain-hardening behaviour, a key factor controlling the overall mechanical performance of such alloys.

2. Materials and Methods

A 60 mm diameter bar of BioDur® 108 alloy was supplied by L. KLEIN SA for this study (marketed under the name Chronifer® 108, UNS S 29108). The material was received in the annealed condition (Condition A). The nominal and analysed chemical compositions are summarized in Table 1.

Table 1. Nominal and analysed chemical composition of BioDur® 108 alloy used in this study.

Chemical Composition (wt.%)	Fe	Mn	Cr	N	Si	Mo	Cu	Others (C, Ni, P, S)
Nominal *	Bal.	21.0–24.0	19.0–23.0	0.85–1.1	max. 0.75	0.5–1.5	max. 0.25	<0.1
Analysed **	Bal.	23.23	21.09	1.01	0.29	0.72	0.04	<0.04

* according to ASTM F 2229 [40]; ** from provided certificate.

Flat dog-bone tensile specimens were machined from slices extracted from the bar such that the loading axis was oriented along the radial or near-radial direction, i.e., perpendicular to the bar longitudinal axis, while the specimen width was parallel to the longitudinal direction. Uniaxial tensile tests were performed at room temperature using an Instron 5966 universal testing machine (Instron, Norwood, MA, USA) equipped with a 10 kN load cell and a 10 mm gauge-length extensometer. The applied strain rate was 10^{-3} s^{-1}. For each condition, two tensile specimens were tested to assess the repeatability of the mechanical response. For clarity, only one representative stress–strain curve is presented for each condition, whereas the main mechanical properties are reported as the mean values ± standard deviation obtained from the two specimens.

Additional slices were cold rolled at room temperature, along the length of the pieces, to thickness reductions of 10%, 20%, 50%, and 70%, after which tensile specimens were also extracted for subsequent characterization.

Miniature tensile specimens with a double-fillet geometry and mirror-polished surface finish were machined for in-situ SEM investigations. In-situ tensile experiments were carried out using a Proxima 100 microtensile testing stage (microMECHA, Kammrath & Weiss GmbH, Schwerte, Germany), equipped with a 3 kN load cell, at a strain rate of 10^{-3} s^{-1}. Electron backscatter diffraction (EBSD) maps were acquired at various deformation stages using a Zeiss Supra 55 field-emission gun scanning electron microscope (FEG-SEM) (Carl Zeiss, Oberkochen, Germany) operated at 20 kV and equipped with an Oxford Instruments Symmetry detector (Oxford Instruments, High Wycombe, UK) controlled by AZtec v6.2 SP1 software.

Schematics illustrating the geometries and dimensions of the different types of tensile specimens used in this study are provided in Figure 1.

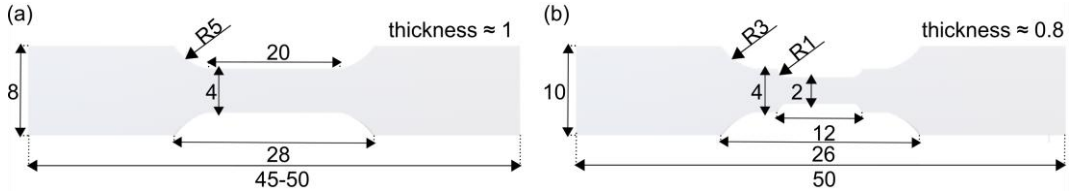


Figure 1. Specimen geometries and dimensions: (**a**) flat dog-bone specimen, and (**b**) in-situ tensile specimen. All dimensions are in millimeters.

Additional conventional microstructural observations were also performed without the in-situ tensile test setup. All EBSD patterns were indexed assuming the austenitic γ-Fe crystal structure (face-centred cubic, space group 225, *Fm*—*3m*). Step sizes of 0.5 μm and 0.2 μm were used for overview and high-magnification scans, respectively. EBSD data

were analysed using AZtecCrystal 3.3 software package. Data clean-up was restricted to removing wild spikes. High-angle grain boundaries (HAGBs) were defined by a misorientation threshold of 15°. Annealing twin boundaries (∑3, 60° <111> within Brandon's criterion) were excluded from the grain boundary network to evaluate grain size, which was quantified in terms of equivalent circle diameter.

For SEM and EBSD analyses, specimen surfaces were prepared by successive grinding with SiC papers up to 2400 grit, followed by polishing with 6 µm, 3 µm, and 1 µm diamond suspensions. Final surface preparation was achieved by vibratory polishing (VibroMet, Struers) using a 0.25 µm OP-S colloidal silica suspension.

Complementary phase identification was performed by X-ray diffraction (XRD) using a Panalytical X'Pert PRO diffractometer (PANalytical, Almelo, The Netherlands) equipped with a Cu Kα radiation source.

3. Results

3.1. Tensile Properties

The engineering stress–strain curves of the BioDur® 108 alloy obtained from tensile tests are displayed in Figure 2a and main mechanical properties are summarized in Table 2. Material was tested in the as-received annealed condition and after cold rolling with thickness reductions of 10%, 20%, 50% and 70%. Despite the precautions taken during specimen preparation and tensile testing, some relatively large standard deviations (>5%) can be observed. These are mainly attributed to the limited number of specimens tested for each condition. Nevertheless, the scatter remains sufficiently limited to allow the mechanical properties to be assessed, the different conditions to be compared, and the trends in their evolution to be discussed. Both the yield strength (YS) and ultimate tensile strength (UTS) increase monotonically with increasing reduction ratio, while the elongation to fracture decreases significantly. The UTS nearly doubles for the 70% cold-rolled condition compared to the annealed state, rising from approximately 1100 MPa to nearly 1900 MPa, while, conversely, the elongation to failure drops sharply from above 60% to below 10% at the same time. Among tested conditions, a pre-deformation of 20% by cold rolling provides a favourable balance of mechanical properties, with a yield strength of about 1150 MPa combined with a total elongation exceeding 30%. Other noticeable fact is that, in the annealed state, the alloy exhibits a pronounced uniform elongation regime and significant strain-hardening capability. Both features progressively diminish with increasing cold-rolling reduction, to the extent that uniform elongation becomes nearly negligible at the highest reduction levels.

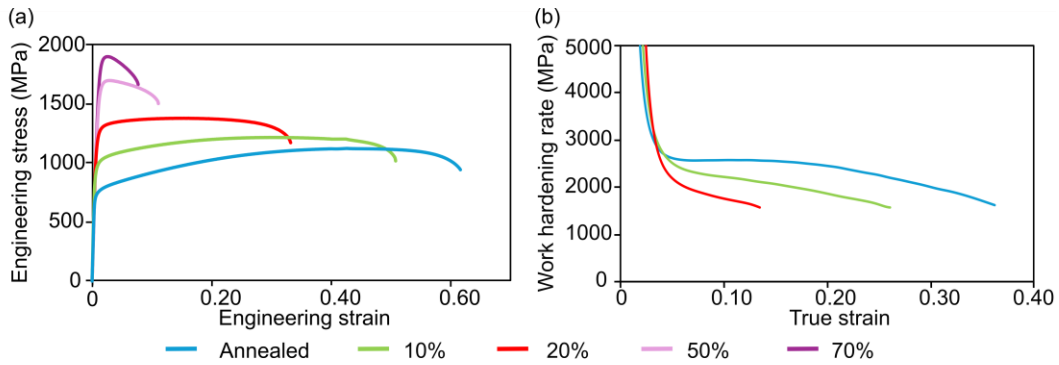


Figure 2. (**a**) Engineering stress–strain curves of the BioDur® 108 alloy in the annealed state and after cold rolling at different thickness reductions; (**b**) corresponding work-hardening-rate curves.

Table 2. Main mechanical properties obtained from tensile tests (mean ± standard deviation).

	Annealed	10%	20%	50%	70%
0.2% Yield strength (MPa)	736 ± 27	911 ± 78	1133 ± 56	1470 ± 23	1640 ± 106
Ultimate tensile strength (MPa)	1068 ± 46	1249 ± 40	1342 ± 49	1690 ± 11	1847 ± 75
Uniform elongation (%)	40 ± 5	27 ± 5	14 ± 5	3 ± 0,1	3 ± 0.1
Elongation at fracture (%)	61 ± 7	45 ± 8	33 ± 3	10 ± 1	8 ± 0.3

Figure 2b presents the corresponding work-hardening-rate curves, obtained as the slope of the true stress–strain curves, and plotted up to the Considère criterion, i.e., when the work-hardening rate equals the true stress ($d\sigma_{true}/d\varepsilon_{true} = \sigma_{true}$), marking the onset of necking. All curves exhibit an initial sharp drop in work-hardening rate, associated with the transition from elastic to plastic deformation. The annealed condition then displays a plateau (up to about 15%), indicative of a nearly constant hardening rate, followed by a gradual decrease. In contrast, the pre-deformed conditions show only a continuously decreasing regime, with no distinct plateau. For pre-deformation levels above 20%, the curves are not shown, as only the initial stage—characterized by an abrupt decrease—was observed, without any subsequent steady-state region.

3.2. Microstructure Evolution

Figure 3 presents the initial microstructure of the BioDur® 108 alloy in the annealed condition. The EBSD orientation map (Figure 3a) reveals equiaxed grains with an average grain size of approximately 58 µm, fully indexed with austenitic γ-Fe FCC structure. The observations show no preferential crystallographic texture. Several relatively wide bands can be observed within the grains, exhibiting 60° misorientation boundaries corresponding to ∑3 grain boundaries, as highlighted in Figure 3b. This confirms that these bands are annealing twins inherited from the heat-treatment process.

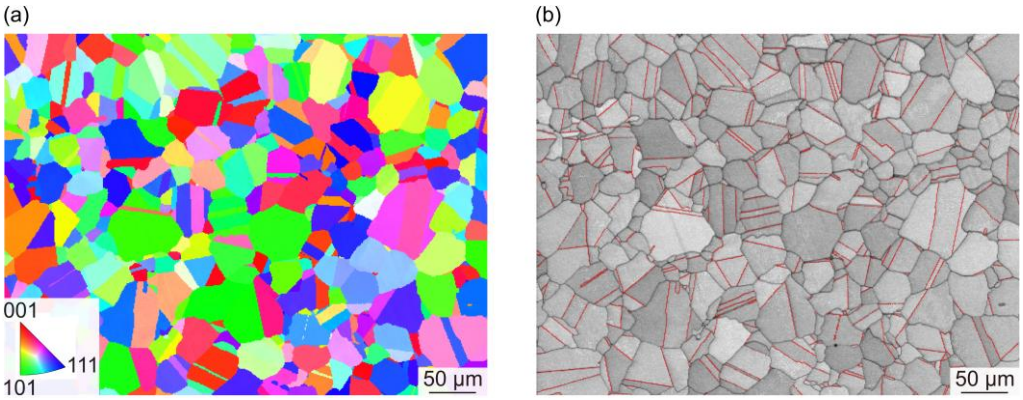


Figure 3. (**a**) EBSD orientation map of the BioDur® 108 alloy in annealed condition; (**b**) corresponding band contrast (BC) map with Σ3 grains boundaries highlighted in red. The standard stereographic triangle used for IPF colour coding is shown in the lower-left corner and applies to all EBSD maps in this article.

An in-situ tensile test was performed inside SEM on this initial state, and the observed microstructural evolution during deformation is shown in Figure 4, which gathers FSD images and EBSD IPF maps acquired at different strain levels (5 stages, numbered 0 to 4 in the present experiment). Stage 0 corresponds to the initial microstructure described previously. At the onset of deformation (stage 1), almost no visible microstructural change is observed. As the strain increases to stage 2, the surface relief becomes more pronounced. In the magnified insets, colour changes within the grains can clearly be observed in the IPF map, indicating local misorientations, together with dark straight lines appearing in the FSD images, which likely correspond to dislocation slip traces. With further

deformation (stage 3), both phenomena become more pronounced: the surface topography increases, the colour gradients become stronger and spread over a larger number of grains, and the slip traces become more numerous. As shown in Figure 5, trace analysis indicates that these observed slip traces correspond to the {111} slip planes.

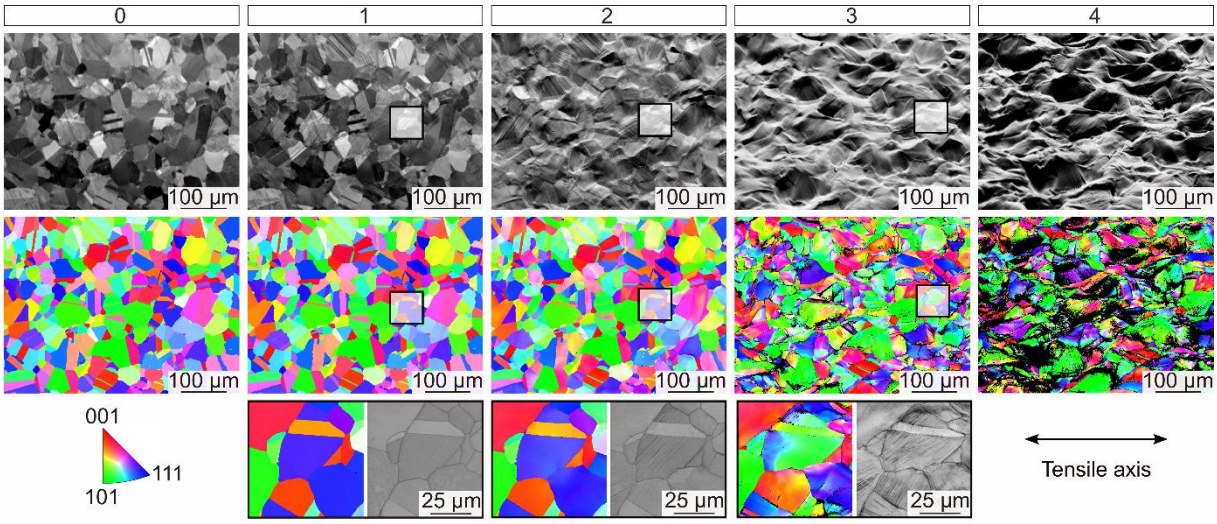


Figure 4. In-situ microstructural characterization of the BioDur® 108 alloy during tensile testing: forescatter electron (FSD) images (grayscale) and EBSD orientation maps (colour) acquired at different strain levels (stages 0 to 4). Magnified views (IPF and BC maps) of the areas marked by white squares are shown at the bottom of each column.

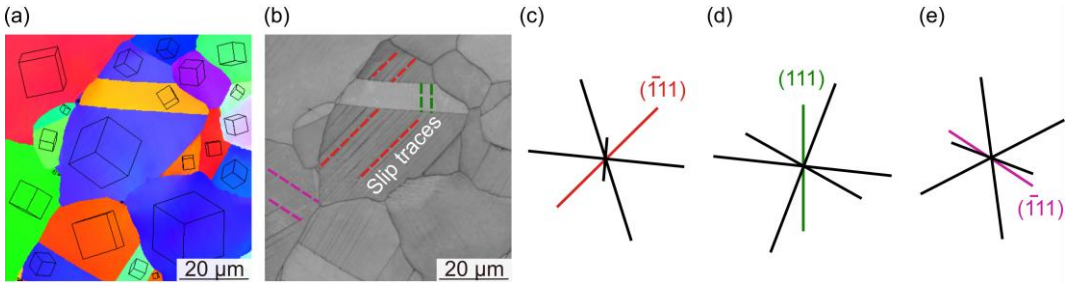


Figure 5. (**a**) EBSD IPF map with visualisations of the austenite crystal orientations. (**b**) BC map showing the experimentally observed slip traces on the alloy surface, with three slip-trace sets highlighted in red, green and pink. (**c**–**e**) Corresponding calculated slip traces for the three {111} plane orientations determined from EBSD orientation data, shown using the same color coding as in (**b**).

At the highest strain level (stage 4), indexing of the microstructure becomes difficult because of the pronounced surface relief and the non-ideal acquisition conditions associated with the in-situ setup, particularly the large working distance. Consequently, the specimen was removed from the in-situ tensile holder, and the same analysed area was subsequently characterized under optimized conditions. The corresponding EBSD analysis is presented in Figure 6. Two areas of interest were selected from the initial region, as indicated by white rectangles in Figure 6a, and higher-magnification EBSD orientation maps were acquired. In these maps (Figure 6b,d), numerous thin bands can be observed within the grains. Despite their narrow thickness, misorientation profiles were extracted across several of these bands. As shown in Figure 6c,e, the band boundaries exhibit a 60° misorientation around the [111] axis relative to the parent grain, corresponding to Σ3 boundaries. Although this misorientation is identical to that of the annealing twins observed in the initial microstructure, their lenticular rather than straight-edged morphology, together with their size and the mechanical history of the specimen, suggests that

these newly formed bands are more likely to correspond to deformation twins generated during tensile loading.

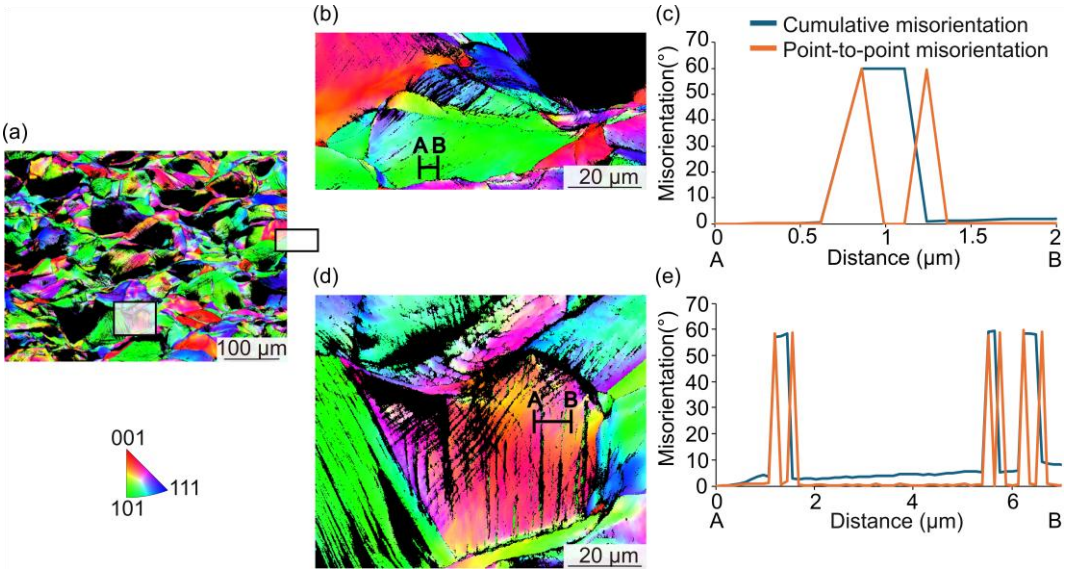


Figure 6. (**a**) EBSD orientation map of the same area as in Figure 4, acquired under improved acquisition conditions after the in-situ tensile test (stage 4); (**b**,**d**) higher-magnification EBSD maps from the areas marked by white squares; (**c**,**e**) corresponding misorientation profiles measured along the AB lines for each area, respectively. The map in (**b**) corresponds to the region highlighted in the zoomed-in insets of Figure 4.

To improve indexing quality, particularly by reducing the surface relief of the specimen, an additional polishing step was performed prior to a new EBSD analysis. As shown in Figure 7a, the amount of non- or poorly indexed areas is significantly reduced. Furthermore, the magnified region and the corresponding misorientation profile presented in Figure 7b,c, respectively, clearly confirm the presence of fine Σ3 deformation twins.

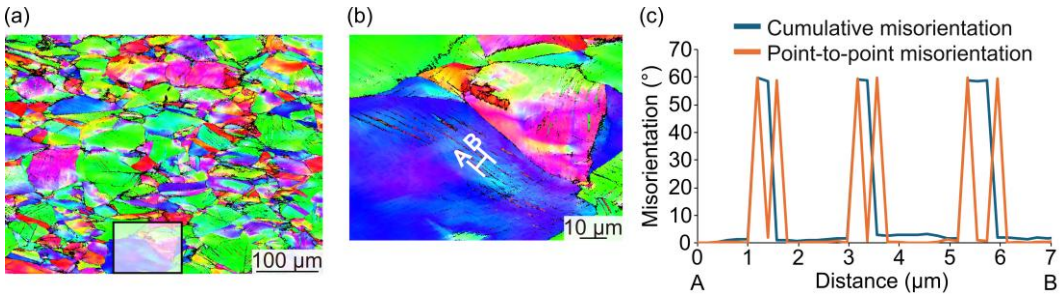


Figure 7. (**a**) EBSD orientation map acquired after post-test polishing of the specimen deformed to stage 4; (**b**) magnified view of the area marked by a white square; (**c**) corresponding misorientation profile measured along the AB line.

Since our experimental setup did not allow precise quantitative monitoring of the strain level, additional experiments were carried out to determine at which stage of deformation these mechanical twins appeared in the material.

A conventional tensile test was interrupted at 15% strain, corresponding to the end of the plateau observed on the work-hardening-rate curve of the annealed condition. The EBSD maps acquired after this test are shown in Figure 8. Fine dark bands, which can appear similar to those previously observed in Figure 6, can be identified. However, their indexing quality is insufficient, preventing any reliable misorientation measurement. As

performed previously, the specimen was subsequently repolished to reduce the roughness induced by tensile deformation and thus improve EBSD indexing quality.

The new EBSD maps obtained after polishing, presented in Figure 9, still reveal local colour gradients associated with local misorientation in some grains, whereas the fine dark lines have clearly disappeared. This indicates that the lines observed prior to polishing mainly originated from surface relief generated by slip bands (topographic and shadowing effects) rather than from an actual microstructural transformation such as twinning. These observations indicate that mechanical twinning is not detected below 15% strain given the sampling and resolution conditions used in this study. Consequently, mechanical twinning does not appear to be responsible for the plateau observed in the work-hardening-rate curve of the BioDur® 108 alloy in annealed condition.

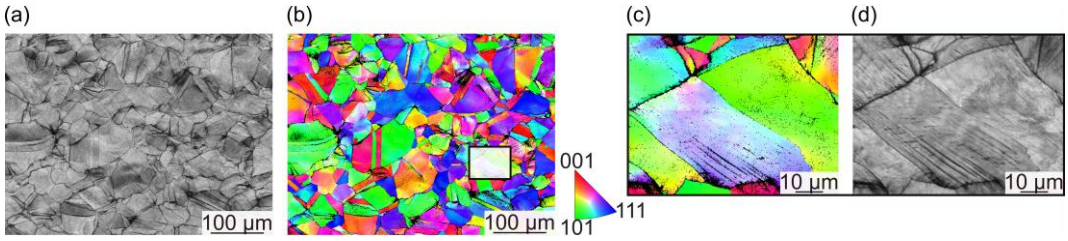


Figure 8. (**a**) BC and (**b**) EBSD orientation maps of a specimen deformed to 15% strain; (**c**,**d**) magnified views (IPF and BC maps) of the area marked by a white square.

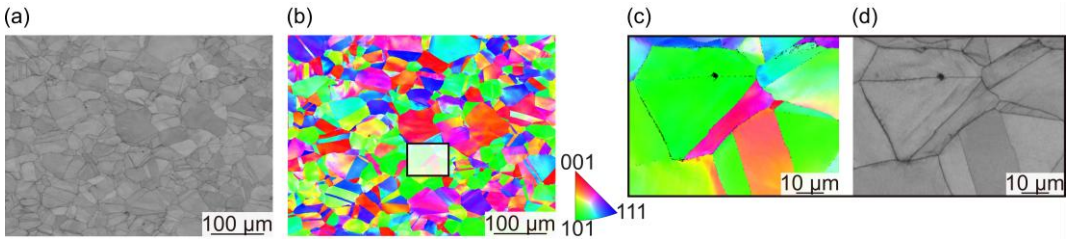


Figure 9. (**a**) BC and (**b**) EBSD orientation maps acquired after post-polishing of the specimen deformed to 15% strain; (**c**,**d**) magnified views (IPF and BC maps) of the area marked by a white square.

3.3. Phase Analysis

Additional XRD analyses were performed on the BioDur® 108 alloy in the annealed state and after cold rolling with thickness reductions of 10%, 20%, 50%, and 70%. The corresponding diffraction patterns are presented in Figure 10. As can be seen, only the FCC austenitic phase is detected in all conditions, and the lattice parameter was estimated to be 3.634 Å. These results are consistent with previous EBSD observations and confirm that the nitrogen content in the BioDur® 108 alloy is sufficiently high to stabilize the austenite and suppress the martensitic transformation, even at high deformation levels. A progressive broadening of the XRD peaks is observed with increasing cold-rolling reduction, which can be mainly attributed to the increase in dislocation density and the associated lattice microstrains induced by plastic deformation, together with the refinement of coherently diffracting domains.

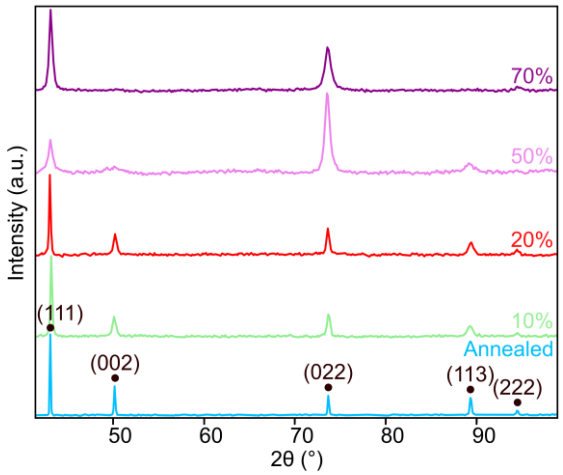


Figure 10. XRD patterns of the BioDur® 108 alloy in the annealed state and after cold rolling at different thickness reductions, indexed with austenite phase. The diffractograms are vertically offset for clarity. Intensity is shown in arbitrary units (a.u.).

4. Discussion

Microstructural investigations indicated that dislocation slip is the dominant deformation mechanism in the BioDur® 108 alloy. Mechanical twinning was observed at relatively high strain levels (>15% elongation) and appeared to represent a minor contribution to the overall deformation. Furthermore, no evidence of strain-induced martensitic transformation was detected, even at the highest investigated strain levels. Consequently, the pronounced work-hardening plateau observed in Figure 2b is unlikely to be governed by TWIP or TRIP mechanisms and appears to arise primarily from dislocation-mediated plasticity.

This quite surprising behaviour can be rationalized by the high nitrogen content of the alloy. Previous studies on high-nitrogen austenitic steels have reported a significant increase in the work-hardening capacity with increasing nitrogen concentration [35,36,43,44]. Nitrogen, as an interstitial solute, exhibits strong chemical interactions with substitutional alloying elements, particularly Cr [29,45–47]. These interactions are widely reported to promote the formation of short-range order (SRO) clusters within the austenitic matrix [31–34,48,49]. Such local atomic ordering can act as an effective barrier to dislocation motion, particularly for deformation mechanisms involving dislocation movement out of the primary slip plane [50,51].

The presence of SRO may increase the energy barrier associated with the constriction and recombination of Shockley partial dislocations, a prerequisite for cross-slip. As a result, cross-slip may be inhibited, thereby suppressing the associated dynamic recovery processes. Plastic deformation is therefore expected to proceed predominantly through localized dislocation glide with limited cross-slip [36,52], consistent with the trace analysis presented in Figure 5. Indeed, the observation of distinct, parallel slip traces corresponding to {111} planes within individual grains indicates that plastic deformation is highly localized on specific slip planes, which is consistent with a planar slip mechanism in the austenitic matrix. This resulting localization of dislocation glide may favour dislocation accumulation on specific slip planes and increase the probability of geometrically compatible interactions between dislocations operating on different slip systems, which may promote the formation of Lomer–Cottrell locks [52]. These sessile dislocation structures can act as effective obstacles to further dislocation motion and may therefore contribute significantly to strain hardening.

The extended work-hardening plateau could therefore be interpreted as the result of sustained dislocation accumulation driven by (i) the continuous generation of new

dislocations, (ii) the progressive accumulation of Lomer–Cottrell locks, and (iii) the limited dynamic recovery associated with restricted cross-slip. Consequently, the alloy retains a high strain-hardening capability over a large strain range, which delays plastic instability and promotes ductility.

The unusual shape of the flow curve can be quantitatively described using the Ludwigson equation. The strain-hardening behaviour of metallic materials is commonly represented by the Hollomon relationship:

$$\sigma = K\varepsilon^n \quad (1)$$

where σ is the true stress, ε is the true plastic strain, K is the strength coefficient, and n is the strain-hardening exponent. However, this equation often fails to accurately describe the deformation behaviour of austenitic stainless steels at low plastic strains [38,53,54]. In the present alloy, as can be seen in Figure 11, the double-logarithmic plot of true stress versus true plastic strain exhibits a clear two-stage hardening behaviour, with a noticeable deviation from the Hollomon law at low strains.

To account for this deviation, the Ludwigson modification introduces an additional term Δ [54]:

$$\sigma = K_1\varepsilon^{n_1} + \Delta = K_1\varepsilon^{n_1} + exp(K_2 + n_2\varepsilon) \quad (2)$$

The parameters K_1 and n_1 were determined from the high-strain region by fitting the Hollomon relationship. The fitting range was selected by considering the largest possible number of experimental data points at the end of the tensile test, before the Considère criterion was reached, while maintaining a coefficient of determination (R^2) above 99.9% (corresponding to a true stress range of 1040–1599 MPa). The parameters K_2 and n_2 were subsequently obtained from the regression of $\ln(\sigma - K_1\varepsilon^{n_1})$ as a function of true strain in the low-strain regime. Similarly, the largest possible number of experimental data points at the beginning of the tensile test was considered, starting from the yield point, while maintaining a coefficient of determination (R^2) above 99.9% (corresponding to a true stress range of 710–1025 MPa). The overall fitting accuracy was estimated to be 99.9%. The transition strain ε_L, corresponding to the strain at which the Ludwigson correction term becomes negligible compared with the Hollomon term, was calculated using:

$$r = exp(K_2 + n_2\varepsilon_L)/(K_1\varepsilon_L^{n_1}) \quad (3)$$

where r is an arbitrary threshold value, fixed at 0.02 according to values reported in the literature [38,53–56]. The resulting transition strain was estimated to be ε_L = 0.12. All fitted parameters are summarized in Table 3.

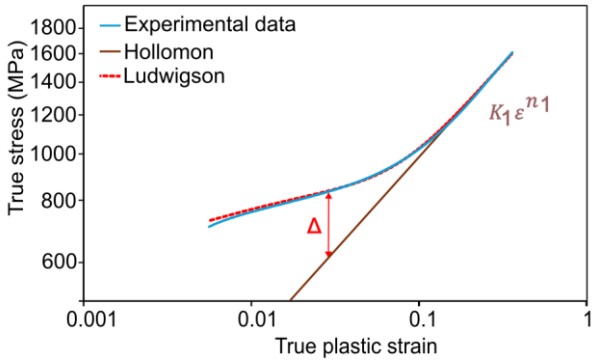


Figure 11. True flow curve of the BioDur® 108 (logarithmic coordinates). Experimental data are plotted in blue and compared to Hollomon (brown line) and Ludwigson (red dotted line) models.

Table 3. Parameters characterizing the true flow curve of the BioDur® 108 alloy obtained from the Ludwigson equation.

K_1 (MPa)	n_1	K_2	n_2	ε_L	σ_L (MPa)
2362.09	0.38	6.18	−25.166	0.12	1061

According to Ludwigson, a larger deviation from the classical Hollomon behaviour is generally associated with deformation modes involving restricted cross-slip and localized dislocation glide, features that are frequently encountered in low-SFE materials. Consequently, the parameters n_2 and ε_L can be regarded as qualitative indicators of the deformation mode. The values obtained in the present study are comparable to those reported for brass and conventional austenitic stainless steels [38,54], suggesting a deformation behaviour more typical of relatively low-SFE materials.

This observation is particularly noteworthy because thermodynamic calculations performed using Thermo-Calc (TCFE14 database) predict a stacking fault energy (SFE) of 51 mJ·m^{-2} for the BioDur® 108 alloy (details and potential limitations of the calculation procedure are provided in the Supplementary Material). This value lies in the upper range typically reported for austenitic stainless steels, and is generally associated with a transition regime where mixed or wavy dislocation slip prevails and cross-slip is expected to be relatively active [57–59].

However, it should be emphasized that SFE values obtained from thermodynamic calculations represent an equilibrium-based estimate and may not fully capture the effective stacking fault energy under deformation [60]. In particular, local chemical ordering, solute–dislocation interactions, and short-range order effects can significantly modify the energy barrier for partial dislocation separation and recombination.

In the present alloy, despite the comparatively high calculated SFE, the deformation behaviour is inconsistent with enhanced cross-slip activity and dynamic recovery typically expected in this regime. Instead, the material exhibits deformation characteristics consistent with strongly restricted cross-slip and localized dislocation glide.

This apparent discrepancy highlights that, in high-nitrogen austenitic steels, and particularly for the special chemical composition of BioDur® 108 alloy, the stacking fault energy alone is not sufficient to rationalize the observed deformation behaviour. Additional microstructural factors, particularly short-range ordering induced by nitrogen, are therefore likely to play a decisive role in controlling dislocation mobility.

These mechanisms explain the unusual and highly attractive combination of mechanical properties exhibited by the alloy, namely a relatively high yield strength, sustained work hardening, and excellent ductility. Combined with its biocompatible and nickel-free chemical composition, these characteristics make the BioDur® 108 alloy a promising candidate for biomedical applications. In particular, the ability to retain substantial ductility while achieving high strength levels suggests that cold-worked conditions could be considered for demanding applications requiring enhanced mechanical performance, such as the ongoing miniaturization of medical devices and implants.

5. Conclusions

The microstructural evolution of the BioDur® 108 alloy during deformation was investigated through EBSD analysis, including in-situ tensile testing. The main conclusions can be summarized as follows:

(1) The high-nitrogen, nickel-free BioDur® 108 alloy exhibits a remarkable combination of high strength, sustained work hardening and good ductility, while retaining a fully stable γ-austenitic structure with no evidence of strain-induced martensitic transformation over the investigated strain range.

(2) Plastic deformation is dominated by dislocation slip, with pronounced slip localization observed during in situ EBSD testing. Mechanical twinning is detected at relatively high strains (>15%) and appears to remain a secondary contribution to the overall deformation. Consequently, the work-hardening behaviour is primarily attributed to dislocation accumulation and strong dislocation interactions rather than TWIP- or TRIP-related mechanisms.

(3) In the annealed state, the work-hardening-rate curve exhibits a pronounced plateau. Ludwigson analysis of the true stress–strain behaviour yields parameters characteristic of deformation modes more commonly associated with low-stacking-fault-energy (SFE) materials.

(4) The combined mechanical and microstructural results are consistent with a mechanism involving nitrogen-induced short-range ordering that limits cross-slip and dynamic recovery. This restricted mobility is expected to promote localized slip and the formation of strong dislocation obstacles such as Lomer–Cottrell locks. Despite a comparatively high calculated stacking fault energy, the alloy exhibits deformation behaviour characteristic of materials with limited cross-slip activity, which suggest that chemical short-range order likely plays a major role in controlling plasticity in this alloy.

Supplementary Materials: The following supporting information can be downloaded at: https://www.mdpi.com/article/10.3390/met16111249/s1. The Supplementary Material provide details on the calculation of the stacking fault energy, as well as its limitations. References [23,28,29,37,61–64] are cited in the Supplementary Materials.

Author Contributions: Conceptualization, S.D. and M.B.; validation, S.D. and F.P.; formal analysis, M.B.; data curation, M.B.; writing—original draft preparation, M.B.; writing—review and editing, S.D. and F.P.; visualization, M.B.; supervision, S.D. and F.P.; project administration, S.D. and F.P.; funding acquisition, S.D. and F.P. All authors have read and agreed to the published version of the manuscript.

Funding: This work was co-funded by the ANRT (Association Nationale de la Recherche et de la Technologie) through a CIFRE industrial PhD fellowship granted to Marine Barrabé (CIFRE No. 2023/0782). The authors declare that this study also received funding from BIOTECH DENTAL company. The funder was not involved in the study design, collection, analysis, interpretation of data, the writing of this article or the decision to submit it for publication.

Data Availability Statement: The original contributions presented in this study are included in the article/supplementary material. Further inquiries can be directed to the corresponding author.

Acknowledgments: The authors would like to thank Manon Bonvalet Rolland for her valuable assistance with the stacking fault energy (SFE) calculations, and Fan Sun and Daniel Galy for their technical support during the in situ tensile testing experiments. The authors are also grateful to Thomas Belforti for contributing to the development of the software used for in situ data analysis.

Conflicts of Interest: Author Marine Barrabé and Stéphanie Delannoy were employed by the company Biotech Dental SAS. The remaining authors declare that the research was conducted in the absence of any commercial or financial relationships that could be construed as a potential conflict of interest.

References

1. Kumar, S.; Mahobia, G.S. Possible Environments for Application of High Nitrogen Nickel Free Stainless Steel: A Review. *Metall. Res. Technol.* **2025**, *122*, 120. https://doi.org/10.1051/metal/2024110.
2. Sumita, M.; Hanawa, T.; Teoh, S.H. Development of Nitrogen-Containing Nickel-Free Austenitic Stainless Steels for Metallic Biomaterials—Review. *Mater. Sci. Eng. C* **2004**, *24*, 753–760. https://doi.org/10.1016/j.msec.2004.08.030.

3. Talha, M.; Behera, C.K.; Sinha, O.P. A Review on Nickel-Free Nitrogen Containing Austenitic Stainless Steels for Biomedical Applications. *Mater. Sci. Eng. C* **2013**, *33*, 3563–3575. https://doi.org/10.1016/j.msec.2013.06.002.
4. Patnaik, L.; Ranjan Maity, S.; Kumar, S. Status of Nickel Free Stainless Steel in Biomedical Field: A Review of Last 10 Years and What Else Can Be Done. *Mater. Today Proc.* **2020**, *26*, 638–643. https://doi.org/10.1016/j.matpr.2019.12.205.
5. Talha, M.; Behera, C.K.; Sinha, O.P. Effect of Nitrogen and Cold Working on Structural and Mechanical Behavior of Ni-Free Nitrogen Containing Austenitic Stainless Steels for Biomedical Applications. *Mater. Sci. Eng. C* **2015**, *47*, 196–203. https://doi.org/10.1016/j.msec.2014.10.078.
6. Yang, K.; Ren, Y. Nickel-Free Austenitic Stainless Steels for Medical Applications. *Sci. Technol. Adv. Mater.* **2010**, *11*, 014105. https://doi.org/10.1088/1468-6996/11/1/014105.
7. Park, J.Y.; Park, S.-J.; Kang, J.-Y.; Lee, C.-H.; Ha, H.-Y.; Moon, J.; Jang, J.H.; Lee, T.-H. Fatigue Behaviors of High Nitrogen Stainless Steels with Different Deformation Modes. *Mater. Sci. Eng. A* **2017**, *682*, 622–628. https://doi.org/10.1016/j.msea.2016.11.053.
8. Kimber, I.; Basketter, D.A. Allergic Sensitization to Nickel and Implanted Metal Devices: A Perspective. *Dermatitis®* **2022**, *33*, 396–404. https://doi.org/10.1097/DER.0000000000000819.
9. Baumann, C.A.; Crist, B.D. Nickel Allergy to Orthopaedic Implants: A Review and Case Series. *J. Clin. Orthop. Trauma* **2020**, *11*, S596–S603. https://doi.org/10.1016/j.jcot.2020.02.008.
10. Schram, S.E.; Warshaw, E.M.; Laumann, A. Nickel Hypersensitivity: A Clinical Review and Call to Action. *Int. J. Dermatol.* **2010**, *49*, 115–125. https://doi.org/10.1111/j.1365-4632.2009.04307.x.
11. Grabke, H.J. The Role of Nitrogen in the Corrosion of Iron and Steels. *ISIJ Int.* **1996**, *36*, 777–786. https://doi.org/10.2355/isijinternational.36.777.
12. Thomann, U.I.; Uggowitzer, P.J. Wear–Corrosion Behavior of Biocompatible Austenitic Stainless Steels. *Wear* **2000**, *239*, 48–58. https://doi.org/10.1016/S0043-1648(99)00372-5.
13. Talha, M.; Behera, C.K.; Sinha, O.P. *In-Vitro* Long Term and Electrochemical Corrosion Resistance of Cold Deformed Nitrogen Containing Austenitic Stainless Steels in Simulated Body Fluid. *Mater. Sci. Eng. C* **2014**, *40*, 455–466. https://doi.org/10.1016/j.msec.2014.04.006.
14. Inoue, M.; Sasaki, M.; Katada, Y.; Taguchi, T. Quantitative Biocompatibility Evaluation of Nickel-Free High-Nitrogen Stainless Steel in Vitro/in Vivo. *J. Biomed. Mater. Res. B Appl. Biomater.* **2014**, *102*, 68–72. https://doi.org/10.1002/jbm.b.32982.
15. Yang, C.; Wang, Q.; Ren, Y.; Jin, D.; Liu, D.; Moradi, M.; Chen, X.; Li, H.; Xu, D.; Wang, F. Corrosion Behavior of High Nitrogen Nickel-Free Austenitic Stainless Steel in the Presence of Artificial Saliva and *Streptococcus mutans*. *Bioelectrochemistry* **2021**, *142*, 107940. https://doi.org/10.1016/j.bioelechem.2021.107940.
16. European Parliament and Council of the European Union. Regulation (EU) 2017/745 of the European Parliament and of the Council of 5 April 2017 on Medical Devices, Amending Directive 2001/83/EC, Regulation (EC) No 178/2002 and Regulation (EC) No 1223/2009 and Repealing Council Directives 90/385/EEC and 93/42/EEC. *Off. J. Eur. Union* **2017**, *L117*, 1–175.
17. Lee, T.-H.; Oh, C.-S.; Kim, S.-J.; Takaki, S. Deformation Twinning in High-Nitrogen Austenitic Stainless Steel. *Acta Mater.* **2007**, *55*, 3649–3662. https://doi.org/10.1016/j.actamat.2007.02.023.
18. Bhav Singh, B.; Sivakumar, K.; Balakrishna Bhat, T. Effect of Cold Rolling on Mechanical Properties and Ballistic Performance of Nitrogen-Alloyed Austenitic Steels. *Int. J. Impact Eng.* **2009**, *36*, 611–620. https://doi.org/10.1016/j.ijimpeng.2008.07.082.
19. Shi, F.; Zhang, X.; Li, T.; Guan, X.; Li, X.; Liu, C. Effects of Nitrogen Content and Strain Rate on the Tensile Behavior of High-Nitrogen and Nickel-Free Austenitic Stainless Steel. *Crystals* **2023**, *13*, 129. https://doi.org/10.3390/cryst13010129.
20. He, Z.; Sun, L.; Guo, Y.; Zhao, J.; Zhang, H.; Jiang, S.; Yan, H.-L.; Zhang, N.; Jia, N. Strengthening High-Nitrogen Austenitic Stainless Steel via Constructing Multi-Scaled Heterostructure. *J. Mater. Res. Technol.* **2024**, *32*, 2076–2085. https://doi.org/10.1016/j.jmrt.2024.08.059.
21. Hong, Y.; Han, C.; Wang, G. Research on Strengthening Mechanisms of High-Nitrogen Austenitic Stainless Steel. *J. Mater. Eng. Perform.* **2025**, *35*, 18708–18714. https://doi.org/10.1007/s11665-025-13021-4.
22. Lee, T.-H.; Shin, E.; Oh, C.-S.; Ha, H.-Y.; Kim, S.-J. Correlation between Stacking Fault Energy and Deformation Microstructure in High-Interstitial-Alloyed Austenitic Steels. *Acta Mater.* **2010**, *58*, 3173–3186. https://doi.org/10.1016/j.actamat.2010.01.056.
23. Mosecker, L.; Saeed-Akbari, A. Nitrogen in Chromium–Manganese Stainless Steels: A Review on the Evaluation of Stacking Fault Energy by Computational Thermodynamics. *Sci. Technol. Adv. Mater.* **2013**, *14*, 033001. https://doi.org/10.1088/1468-6996/14/3/033001.
24. Kibey, S.; Liu, J.B.; Curtis, M.J.; Johnson, D.D.; Sehitoglu, H. Effect of Nitrogen on Generalized Stacking Fault Energy and Stacking Fault Widths in High Nitrogen Steels. *Acta Mater.* **2006**, *54*, 2991–3001. https://doi.org/10.1016/j.actamat.2006.02.048.

25. Gavriljuk, V.; Petrov, Y.; Shanina, B. Effect of Nitrogen on the Electron Structure and Stacking Fault Energy in Austenitic Steels. *Scr. Mater.* **2006**, *55*, 537–540. https://doi.org/10.1016/j.scriptamat.2006.05.025.
26. Ojima, M.; Adachi, Y.; Tomota, Y.; Katada, Y.; Kaneko, Y.; Kuroda, K.; Saka, H. Weak Beam TEM Study on Stacking Fault Energy of High Nitrogen Steels. *Steel Res. Int.* **2009**, *80*, 477–481. https://doi.org/10.2374/SRI09SP038.
27. Das, A. Revisiting Stacking Fault Energy of Steels. *Metall. Mater. Trans. A* **2016**, *47*, 748–768. https://doi.org/10.1007/s11661-015-3266-9.
28. Lee, S.-J.; Fujii, H.; Ushioda, K. Thermodynamic Calculation of the Stacking Fault Energy in Fe-Cr-Mn-C-N Steels. *J. Alloys Compd.* **2018**, *749*, 776–782. https://doi.org/10.1016/j.jallcom.2018.03.296.
29. Kim, J.-M.; Kim, S.-J.; Kang, J.-H. Effects of Short-Range Ordering and Stacking Fault Energy on Tensile Behavior of Nitrogen-Containing Austenitic Stainless Steels. *Mater. Sci. Eng. A* **2022**, *836*, 142730. https://doi.org/10.1016/j.msea.2022.142730.
30. Terazawa, Y.; Ando, T.; Tsuchiyama, T.; Takaki, S. Relationship between Work Hardening Behaviour and Deformation Structure in Ni-Free High Nitrogen Austenitic Stainless Steels. *Steel Res. Int.* **2009**, *80*, 473–476. https://doi.org/10.2374/SRI09SP039.
31. Gavriljuk, V.G.; Berns, H. *High Nitrogen Steels: Structure, Properties, Manufacture, Applications*; Springer: Berlin/Heidelberg, Germany, 1999; pp. 1–71, ISBN 978-3-642-08567-3.
32. Karaman, I.; Sehitoglu, H.; Chumlyakov, Y.I.; Maier, H.J. The Deformation of Low-Stacking-Fault-Energy Austenitic Steels. *JOM* **2002**, *54*, 31–37. https://doi.org/10.1007/BF02700983.
33. Milititsky, M.; De Wispelaere, N.; Petrov, R.; Ramos, J.E.; Reguly, A.; Hänninen, H. Characterization of the Mechanical Properties of Low-Nickel Austenitic Stainless Steels. *Mater. Sci. Eng. A* **2008**, *498*, 289–295. https://doi.org/10.1016/j.msea.2008.08.012.
34. Kawahara, Y.; Masumura, T.; Koyano, T.; Tsuchiyama, T. Deformation Structure of Chromium-Free High-Nitrogen Austenite in Fe–N Binary Alloys. *ISIJ Int.* **2026**, *66*, 293–300. https://doi.org/10.2355/isijinternational.ISIJINT-2025-374.
35. Molnár, D.; Lu, S.; Hertzman, S.; Engberg, G.; Vitos, L. Study of the Alternative Mechanism behind the Constant Strain Hardening Rate in High-nitrogen Steels. *Mater. Charact.* **2020**, *170*, 110726. https://doi.org/10.1016/j.matchar.2020.110726.
36. Masumura, T.; Seto, Y.; Tsuchiyama, T.; Kimura, K. Work-Hardening Mechanism in High-Nitrogen Austenitic Stainless Steel. *Mater. Trans.* **2020**, *61*, 678–684. https://doi.org/10.2320/matertrans.H-M2020804.
37. Mosecker, L.; Pierce, D.T.; Schwedt, A.; Beighmohamadi, M.; Mayer, J.; Bleck, W.; Wittig, J.E. Temperature Effect on Deformation Mechanisms and Mechanical Properties of a High Manganese C+N Alloyed Austenitic Stainless Steel. *Mater. Sci. Eng. A* **2015**, *642*, 71–83. https://doi.org/10.1016/j.msea.2015.06.047.
38. Sun, G.; Yu, A.; Sun, S.; Ji, C.; Jiang, Z.; Lian, J. Plastic Deformation and Fracture Behaviour of High-Nitrogen Nickel-Free Austenitic Stainless Steel. *Mater. Sci. Technol.* **2017**, *33*, 1635–1644. https://doi.org/10.1080/02670836.2017.1306012.
39. Wang, S.; Yang, K.; Shan, Y.; Li, L. Plastic Deformation and Fracture Behaviors of Nitrogen-Alloyed Austenitic Stainless Steels. *Mater. Sci. Eng. A* **2008**, *490*, 95–104. https://doi.org/10.1016/j.msea.2008.01.015.
40. *ASTM F 2229-12*; Standard Specification for Wrought, Nitrogen Strengthened 23Manganese-21Chromium-1Molybdenum Low-Nickel Stainless Steel Alloy Bar and Wire for Surgical Implants (UNS S29108). ASTM International: West Conshohocken, PA, USA, 2012.
41. Siredey-Schwaller, N.; Charbonnier, P.; Zhang, Y.; Guyon, J.; Perroud, O.; Laheurte, P. Secondary Hardening of a High-N Ni-Free Stainless Steel. *Materials* **2022**, *15*, 7505. https://doi.org/10.3390/ma15217505.
42. Carpenter Technology Corporation. BioDur®108 Stainless. Available online: https://www.carpentertechnology.com/hubfs/Data%20Sheets/BioDur_108_Stainless_Datasheet.pdf (accessed on 5 October 2023).
43. Saller, G.; Spiradek-Hahn, K.; Scheu, C.; Clemens, H. Microstructural Evolution of Cr–Mn–N Austenitic Steels during Cold Work Hardening. *Mater. Sci. Eng. A* **2006**, *427*, 246–254. https://doi.org/10.1016/j.msea.2006.04.020.
44. Ojima, M.; Adachi, Y.; Tomota, Y.; Ikeda, K.; Kamiyama, T.; Katada, Y. Work Hardening Mechanism in High Nitrogen Austenitic Steel Studied by *in Situ* Neutron Diffraction and *in Situ* Electron Backscattering Diffraction. *Mater. Sci. Eng. A* **2009**, *527*, 16–24. https://doi.org/10.1016/j.msea.2009.07.066.
45. Xie, Y.; Miyamoto, G.; Furuhara, T. Nanosized Cr-N Clustering in Expanded Austenite Layer of Low Temperature Plasma-Nitrided Fe-35Ni-10Cr Alloy. *Scr. Mater.* **2022**, *213*, 114637. https://doi.org/10.1016/j.scriptamat.2022.114637.
46. Xie, Y.; Miyamoto, G.; Furuhara, T. High-Throughput Investigation of Cr-N Cluster Formation in Fe-35Ni-Cr System during Low-Temperature Nitriding. *Acta Mater.* **2023**, *253*, 118921. https://doi.org/10.1016/j.actamat.2023.118921.
47. Sozinov, A.L.; Gavriljuk, V.G. Estimation of Interaction Energies Me-(C, N) in f.c.c. Iron-Based Alloys Using Thermo-Calc Thermodynamic Database. *Scr. Mater.* **1999**, *41*, 679–683. https://doi.org/10.1016/S1359-6462(99)00107-4.
48. Zhou, X.W.; Grujicic, M. Thermodynamic Analysis of the Short Range Order Strengthening in Fe Ni Cr N Austenite. *Calphad* **1996**, *20*, 257–272. https://doi.org/10.1016/S0364-5916(96)00029-6.

49. Grujicic, M.; Zhou, X.W.; Owen, W.S. Monte Carlo Analysis of Short-Range Order in Nitrogen-Strengthened Fe Ni Cr N Austenitic Alloys. *Mater. Sci. Eng. A* **1993**, *169*, 103–110. https://doi.org/10.1016/0921-5093(93)90604-D.
50. Lo, K.H.; Shek, C.H.; Lai, J.K.L. Recent Developments in Stainless Steels. *Mater. Sci. Eng. R Rep.* **2009**, *65*, 39–104. https://doi.org/10.1016/j.mser.2009.03.001.
51. Byrnes, M.L.G.; Grujicic, M.; Owen, W.S. Nitrogen Strengthening of a Stable Austenitic Stainless Steel. *Acta Metall.* **1987**, *35*, 1853–1862. https://doi.org/10.1016/0001-6160(87)90131-3.
52. Kubota, S.; Xia, Y.; Tomota, Y. Work-Hardening Behavior and Evolution of Dislocation-Microstructures in High-Nitrogen Bearing Austenitic Steels. *ISIJ Int.* **1998**, *38*, 474–481. https://doi.org/10.2355/isijinternational.38.474.
53. Simmons, J.W. Strain Hardening and Plastic Flow Properties of Nitrogen-Alloyed Fe-17Cr-(8–10)Mn-5Ni Austenitic Stainless Steels. *Acta Mater.* **1997**, *45*, 2467–2475. https://doi.org/10.1016/S1359-6454(96)00343-6.
54. Ludwigson, D.C. Modified Stress-Strain Relation for FCC Metals and Alloys. *Metall. Trans.* **1971**, *2*, 2825–2828. https://doi.org/10.1007/BF02813258.
55. Soussan, A.; Degallaix, S.; Magnin, T. Work-Hardening Behaviour of Nitrogen-Alloyed Austenitic Stainless Steels. *Mater. Sci. Eng. A* **1991**, *142*, 169–176. https://doi.org/10.1016/0921-5093(91)90655-7.
56. Li, H.; Jiang, Z.; Zhang, Z.; Xu, B.; Liu, F. Mechanical Properties of Nickel Free High Nitrogen Austenitic Stainless Steels. *J. Iron Steel Res. Int.* **2007**, *14*, 330–334. https://doi.org/10.1016/S1006-706X(08)60105-3.
57. Schramm, R.E.; Reed, R.P. Stacking Fault Energies of Seven Commercial Austenitic Stainless Steels. *Metall. Trans. A* **1975**, *6*, 1345–1351. https://doi.org/10.1007/BF02641927.
58. Brofman, P.J.; Ansell, G.S. On the Effect of Carbon on the Stacking Fault Energy of Austenitic Stainless Steels. *Metall. Trans. A* **1978**, *9*, 879–880. https://doi.org/10.1007/BF02649799.
59. Lu, J.; Hultman, L.; Holmström, E.; Antonsson, K.H.; Grehk, M.; Li, W.; Vitos, L.; Golpayegani, A. Stacking Fault Energies in Austenitic Stainless Steels. *Acta Mater.* **2016**, *111*, 39–46. https://doi.org/10.1016/j.actamat.2016.03.042.
60. Wang, X.; Xiong, W. Stacking Fault Energy Prediction for Austenitic Steels: Thermodynamic Modeling vs. Machine Learning. *Sci. Technol. Adv. Mater.* **2020**, *21*, 626–634. https://doi.org/10.1080/14686996.2020.1808433.
61. Olson, G.B.; Cohen, M. A General Mechanism of Martensitic Nucleation: Part I. General Concepts and the FCC → HCP Transformation. *Metall. Trans. A* **1976**, *7*, 1897–1904. https://doi.org/10.1007/BF02659822.
62. Allain, S.; Chateau, J.-P.; Bouaziz, O.; Migot, S.; Guelton, N. Correlations between the Calculated Stacking Fault Energy and the Plasticity Mechanisms in Fe–Mn–C Alloys. *Mater. Sci. Eng. A* **2004**, *387–389*, 158–162. https://doi.org/10.1016/j.msea.2004.01.059.
63. Curtze, S.; Kuokkala, V.-T.; Oikari, A.; Talonen, J.; Hänninen, H. Thermodynamic Modeling of the Stacking Fault Energy of Austenitic Steels. *Acta Mater.* **2011**, *59*, 1068–1076. https://doi.org/10.1016/j.actamat.2010.10.037.
64. Saeed-Akbari, A.; Imlau, J.; Prahl, U.; Bleck, W. Derivation and Variation in Composition-Dependent Stacking Fault Energy Maps Based on Subregular Solution Model in High-Manganese Steels. *Metall. Mater. Trans. A* **2009**, *40*, 3076–3090. https://doi.org/10.1007/s11661-009-0050-8.

Disclaimer/Publisher's Note: The statements, opinions and data contained in all publications are solely those of the individual author(s) and contributor(s) and not of MDPI and/or the editor(s). MDPI and/or the editor(s) disclaim responsibility for any injury to people or property resulting from any ideas, methods, instructions or products referred to in the content.